



On the competition between synchronous oxidation and preferential oxidation in Cu-Zr-Al metallic glasses

Yifei Xu^a, Lars P.H. Jeurgens^b, Hong Bo^c, Luchan Lin^b, Shengli Zhu^a, Yuan Huang^a, Yongchang Liu^a, Junwei Qiao^d, Zumin Wang^{a,*}

^a School of Materials Science and Engineering, Tianjin University, Tianjin 300350, China

^b Empa, Swiss Federal Laboratories for Materials Science and Technology, Laboratory for Joining Technologies and Corrosion, Ueberlandstrasse 129, 8600 Dübendorf, Switzerland

^c State Key Laboratory of Metastable Materials Science and Technology, and College of Materials Science and Engineering, Yanshan University, Qinhuangdao, Hebei 066004, China

^d College of Materials Science and Engineering, Taiyuan University of Technology, Taiyuan, 030024, China



ARTICLE INFO

Keywords:

Synchronous oxidation
Preferential oxidation
Amorphous alloys
Cu-Zr-Al
Oxidation kinetics

ABSTRACT

The competition between synchronous oxidation and preferential oxidation of Zr and Al in amorphous Cu-Zr-Al alloys has been investigated. Oxide-layer growth on Cu-poor Cu-Zr-Al alloys occurs by synchronous oxidation of Zr and Al. However, for relatively high Cu alloying contents, synchronous oxidation of Zr and Al becomes disturbed by the increased chemical interaction of Cu with Al, which immobilizes Cu and Al atoms from oxidation. Consequently, only Zr is preferentially oxidized. The findings provide fundamental insights on the role of nobler alloy constituents on the oxidation mechanism of multi-component alloys, which opens new avenues for rational design of surficial oxide structures.

1. Introduction

Amorphous alloys have demonstrated exceptional mechanical, chemical and biochemical properties, due to the structural and compositional homogeneity as compared to their crystalline counterparts. Therefore, amorphous alloys are considered as a promising new family of structural and functional materials [1–7]. Amorphous Cu-Zr-Al alloys are one of the most attractive amorphous alloys, because of their very high glass forming ability (GFA) and high formability [8–13], which makes them especially suitable for the fabrication of micro/nano-sized components [14].

Oxidation occurs inevitably during the service of such micro/nano-sized alloy components, thereby affecting their surface properties [15–19]. Controlled pre-oxidation treatments of the fabricated alloys can be performed to tune and stabilize surface-related properties in an efficient and economical way [20, 21]. The oxidation of crystalline ternary metallic alloys has been studied intensively in the past decades. In contrast, much less is known on the oxidation of ternary amorphous metallic alloys. In particular, the compositional changes and inherent metastability of such amorphous alloys during the oxidation process have remained largely unclear. To this end, it is crucial to understand

the underlying oxidation mechanism of multi-component amorphous alloys.

Several studies on the oxidation of amorphous Zr-Al [22–27], Cu-Zr [28–33] and even Cu-Al [34–36] binary alloys have been reported in the literature. Cu-Zr binary alloys have the greatest glass-forming ability [37] among these three alloy systems. During the oxidation of amorphous Cu-Zr binary alloys, Zr has a much larger O affinity than Cu, resulting in the overgrowth of an amorphous ZrO₂ overlayer by the preferential oxidation of Zr [29, 30]. For amorphous Zr-Al binary alloys with medium GFA, synchronous oxidation of Zr and Al results in the formation of a single ternary amorphous Zr-Al-O oxide phase with a fixed composition of (Zr_{0.67}Al_{0.33})O_{1.83}, independent of the parent Zr-Al alloy composition (Zr_{74at.%}Al_{26at.%}–Zr_{32at.%}Al_{68at.%}), which is thermodynamically preferred [25]. Due to their very poor glass-forming ability [38–42], thermal oxidation studies of amorphous Cu-Al binary alloys have not yet been reported. However, Al has a much higher affinity for O than Cu, suggesting the preferential formation of Al₂O₃ from the alloy, as indeed observed for oxidation studies of their crystalline Cu-Al counterparts [34, 36].

For amorphous Cu-Zr-Al ternary alloys, it is not straightforward to rationalize if Zr and Al will be synchronously or preferentially oxidized,

* Corresponding author.

E-mail address: z.wang@tju.edu.cn (Z. Wang).

depending on the alloy composition. For example, for amorphous Cu-Zr-Al ternary alloys with a relatively low Al content of 10 at. %, thermal oxidation is known to result in a double-layered structure, consisting of a tiny Al interfacial oxide layer and a Zr oxide top layer, depending on the oxidation temperature [43–49]. Based on the previous oxidation studies of Al₂Zr binary alloys [22,25,50], it may be presumed that thermal oxidation of amorphous Cu-Zr-Al ternary alloys with a similar Al/Zr atomic ratio of ½ should also result in the formation of a stable amorphous (Zr_{0.67}Al_{0.33})O_{1.83} passive layer by synchronous oxidation of Zr and Al (since Cu has a much lower oxygen affinity). To experimentally verify this hypothesis, the thermal oxidation of amorphous Cu-Zr-Al ternary alloys were investigated as function of the nominal composition, while superimposing the following two criteria: (i) the Al:Zr atomic ratio of the alloys is fixed at 0.5 with varying Cu content, and (ii) the alloys should possess a good GFA. On the basis of these two criteria, three different compositions with Cu concentrations in the range of 25–50 at. % were considered in this study, i.e. Cu_x(Zr_{0.67}Al_{0.33})_{100-x} with $x = 25, 40 [51]. The addition of Cu can greatly promote the GFA of Zr-based alloys, facilitating the formation of bulk metallic glasses (BMG) [13,52,53]. The amorphous Cu_x(Zr_{0.67}Al_{0.33})_{100-x} ($25 \leq x \leq 50$) alloys were thermally oxidized in the temperature range of 250–350 °C. A combinatorial analytical approach by X-ray diffraction (XRD), differential scanning calorimetry (DSC), thermogravimetric analysis (TGA), Auger sputter depth profiling (AES) and cross-sectional high resolution transmission electron microscopy (HRTEM) was applied to study the oxide-layer microstructures, the compositional changes in the alloy and oxide-film growth kinetics as function of the alloy composition. As such, the commonly disregarded role of nobler alloying constituents on the oxidation behaviors of multi-component BMGs could be revealed. The results can provide practical guidelines on the selection of oxidation conditions to tailor the microstructure of protective amorphous oxide layers formed on BMGs.$

2. Experimental

2.1. Specimen preparation and thermal oxidation

Amorphous Cu_x(Zr_{0.67}Al_{0.33})_{100-x} ($25 \leq x \leq 50$) alloy ribbons with a thickness of 35–45 µm and a width of 0.8–1.7 mm were prepared by arc melting the mixtures of pure Cu (purity 99.95 wt. %), Zr (purity 98.5 wt. %) and Al (purity 99.99 wt. %) in an argon atmosphere (99.999 vol. %), and subsequent melt-spinning using a single copper wheel at a surficial linear speed of ~30 m/s. The compositions of the amorphous Cu_x(Zr_{0.67}Al_{0.33})_{100-x} ($25 \leq x \leq 50$) alloys have been verified by inductively coupled plasma optical emission spectroscopy (ICP-OES). The thus prepared amorphous Cu_x(Zr_{0.67}Al_{0.33})_{100-x} ($x = 25, 40) alloys are designated below as am-Cu25, am-Cu40 and am-Cu50, respectively.$

The amorphous Cu_x(Zr_{0.67}Al_{0.33})_{100-x} ($25 \leq x \leq 50$) ribbons were sealed in quartz tubes for subsequent thermal oxidation in a vacuum sealing system (MRVS-3002, Partulab Technology Co. Ltd). The tubes were first evacuated (base pressure ~1 Pa) and then backfilled with pure oxygen gas (purity 99.999 vol. %) for several cycles. The oxygen partial pressures at room temperature were 0.56, 0.52, and 0.47 bar, corresponding to 1 bar at 250, 300 and 350 °C, respectively. The amorphous Cu_x(Zr_{0.67}Al_{0.33})_{100-x} ($25 \leq x \leq 50$) alloys were isothermally oxidized at 250–300 °C in a tube furnace (OTF-1200X, Hefei Kejing Materials Technology Co. Ltd.) for 2.5–10 h and quenched immediately in water after the thermal oxidation.

An Au marker experiment was designed to clarify the atomic transport mechanism for the oxidation of the amorphous Cu_x(Zr_{0.67}Al_{0.33})_{100-x} ($25 \leq x \leq 50$) alloys. To this end, an ultra-thin (thickness 2–3 nm) Au film was deposited on the amorphous Cu_x(Zr_{0.67}Al_{0.33})_{100-x} ($25 \leq x \leq 50$) alloys by magnetron sputtering of pure Au (purity 99.999 wt. %) in a high-vacuum sputter system (employing a target power of 16 W for 1 min). The ribbons were sputter-cleaned for 5 min by Ar⁺ ions with an applied acceleration voltage of 105 V prior to the layer-

deposition process. The Au-covered amorphous Cu_x(Zr_{0.67}Al_{0.33})_{100-x} ($25 \leq x \leq 50$) alloys were then oxidized at 350 °C for 2.5 h, as described above.

2.2. Microstructural analysis

The as-spun and oxidized Cu_x(Zr_{0.67}Al_{0.33})_{100-x} ($25 \leq x \leq 50$) ribbons were investigated by X-ray diffraction (XRD) on a Bruker D8 Advanced diffractometer equipped with a Cu X-ray anode (40 kV/40 mA, $\lambda = 1.5418 \text{ \AA}$). The scanning range of the diffraction angle 2θ is 10–60° with a step size of 0.02° and a collecting time of 0.2 s/step.

Thermal analyses of the as-spun Cu_x(Zr_{0.67}Al_{0.33})_{100-x} ($25 \leq x \leq 50$) ribbons were carried out in a differential scanning calorimeter (DSC, Mettler Toledo TGA/DSC1 Star System) at a heating rate of 10 °C/min under an argon protective atmosphere with a flow rate of 50 cm³/min.

The oxidation kinetics of the as-spun Cu_x(Zr_{0.67}Al_{0.33})_{100-x} ($25 \leq x \leq 50$) ribbons was investigated by thermogravimetric analysis (TGA, Mettler Toledo TGA/DSC1 Star System). The initial weight of the as-spun am-Cu_x(Zr_{0.67}Al_{0.33})_{100-x} ($25 \leq x \leq 50$) ribbons was ~50 mg. Argon protective gas (purity 99.999 vol. %) was introduced into the TGA furnace at a flow rate of 50 cm³/min while heating up the specimens to 300 °C at a rate of 40 °C/min. Subsequently, the isothermal oxidation of the specimens was performed at 300 °C in pure O₂ (purity ≥ 99.999 vol. %), as introduced into the furnace at a constant flow rate of 60 cm³/min.

The oxidized Cu_x(Zr_{0.67}Al_{0.33})_{100-x} ($25 \leq x \leq 50$) ribbons were investigated by Auger electron spectroscopy (AES) sputter-depth profiling using a PHI 700Xi scanning Auger nanoprobe (base pressure ~5 × 10⁻⁷ Pa), equipped with a field-emission electron gun operated at an acceleration voltage of 5 kV. Sputter-depth profiling was performed using 2 kV Ar⁺ ion sputtering cycles. The spectra of the Cu LMM, Zr MNN, Al KLL and O KLL Auger electrons were recorded after each successive sputter step. The concentration-depth profiles of oxidic Zr and Al in the oxide overlayer (denoted as: Zr^{ox} and Al^{ox}), as well as of metallic Zr and Al in the alloy substrate (denoted as: Zr^{met} and Al^{met}), were obtained from the peak-to-peak intensities as resolved by linear least-squares (LLS) fitting of the corresponding differential AES spectra in the Multi-Pak software (v 9.5.0.8). Quantifications of the thus-resolved Zr^{ox}, Al^{ox}, Zr^{met} and Al^{met} intensities, as well as of Cu and O, were carried out according to the procedure as described in Ref. [26]. The correspondingly determined relative sensitivity factors S (with respect to Zr^{met}) are: $S_{\text{Zr}^{\text{met}}} = 1.000$, $S_{\text{Zr}^{\text{ox}}} = 0.626$, $S_{\text{Al}^{\text{met}}} = 0.178$, $S_{\text{Al}^{\text{ox}}} = 0.411$, $S_{\text{Cu}} = 0.408$, and $S_{\text{O}} = 1.324$. The sputtering rate was calibrated using the calibrated oxide-layer thickness, as determined by cross-sectional TEM.

Focused ion beam (FIB) (ZEISS Helios FIB/SEM crossbeam system) was used to prepare cross-sectional TEM lamellae of the oxidized specimens. To protect the lamella area from excessive beam damage during focused ion beam milling, a Pt layer of 500 nm followed by a second Pt layer of ~2 µm were deposited on the area of interest by electron beam and ion beam assisted deposition from gas precursors, respectively. The lamellae were thinned to a thickness of ~1.5 µm before being removed from the bulk specimen using an in-situ lift-out technique. Finally, the lamellae were welded to a Cu grid and further thinned by 30 kV/80–790 pA Ga⁺ ions, followed by cleaning with 5 keV/41 pA (90 s) and 2 keV/23 pA (30 s) Ga⁺ ions.

The composition and microstructure of the oxide overlayers were investigated by cross-sectional transmission electron microscopy (TEM) using a FEI JEOL2200FS electron microscope equipped with a field emission gun, operated at an acceleration voltage of 200 kV. The elemental distributions in the oxide cross-sections were investigated by energy dispersive X-ray spectroscopy (EDX) mapping inside the same microscope.

3. Results

3.1. Microstructure of the as-prepared and oxidized alloys by XRD and DSC

XRD patterns of the as-spun and the oxidized (350°C , 10 h) am-Cu25, am-Cu40 and am-Cu50 alloys are shown in Fig. 1a and b, respectively. Only broad intensity humps with a 2θ range of $32\text{--}47^{\circ}$ and a FWHM of $4.2\text{--}5.5^{\circ}$ are observed in the XRD patterns, confirming the amorphous state of the as-spun alloys (see Fig. 1a). Notably, the position of the intensity hump exhibits a small shift to higher 2θ with increasing

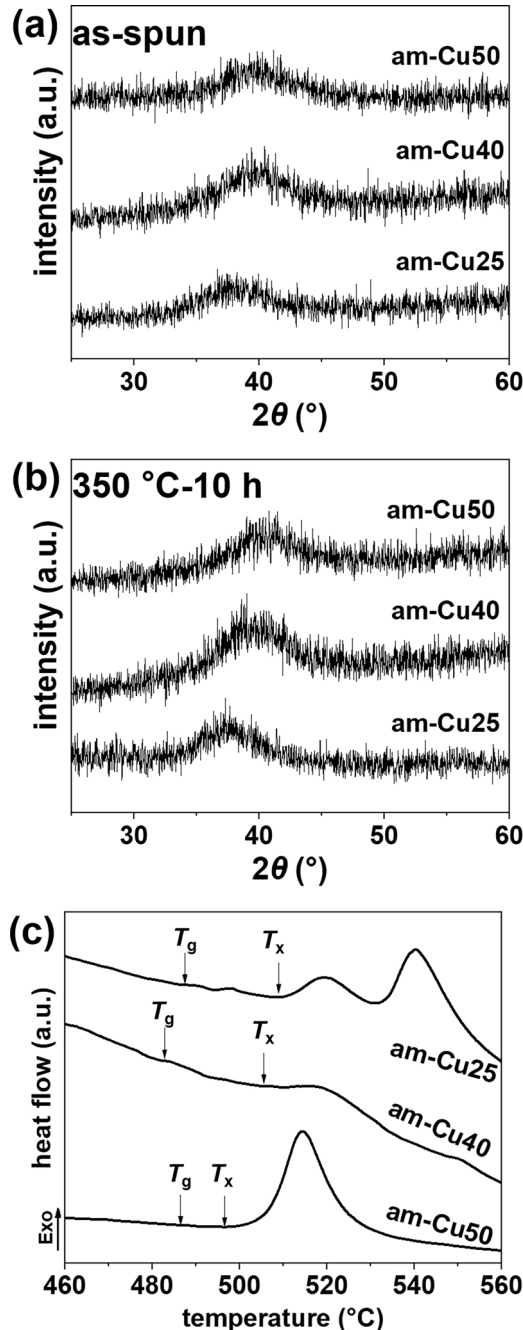


Fig. 1. XRD patterns of $\text{am-Cu}_x(\text{Zr}_{0.67}\text{Al}_{0.33})_{100-x}$ alloys ($25 \leq x \leq 50$) (a) as-spun and (b) oxidized at 350°C for 10 h, and (c) DSC curves of $\text{am-Cu}_x(\text{Zr}_{0.67}\text{Al}_{0.33})_{100-x}$ alloys ($25 \leq x \leq 50$) at a heating rate of $10^{\circ}\text{C}/\text{min}$. The glass transition temperatures T_g and crystallization temperatures T_x are marked by arrows.

Cu content in the alloy. Cross-sectional TEM investigations also evidence the amorphous state of the as-spun alloys (see Sect. 3.4). Moreover, XRD analysis of the oxidized am-Cu_x(Zr_{0.67}Al_{0.33})_{100-x} ($25 \leq x \leq 50$) alloys indicate that the alloys all remain XRD amorphous after prolonged oxidation (10 h) at the highest oxidation temperature of 350°C (see Fig. 1b).

As follows from the DSC analysis (see Fig. 1c), the glass transition temperatures (T_g) and the crystallization temperatures (T_x) are 488°C and 509°C for am-Cu25, 483°C and 506°C for am-Cu40, and 487°C and 497°C for am-Cu50, respectively (see Table 1). The corresponding supercooled liquid regimes, ΔT ($\Delta T = T_x - T_g$), are 21°C , 23°C and 10°C for the am-Cu25, am-Cu40 and am-Cu50 alloy, respectively (see Table 1); this suggests slightly better GFA for am-Cu25 and am-Cu40, as compared to am-Cu50. According to the DSC analysis, thermal oxidation in the temperature range of $250\text{--}350^{\circ}\text{C}$ does not induce crystallization of the studied am-Cu_x(Zr_{0.67}Al_{0.33})_{100-x} alloys, in accordance with the XRD analysis.

3.2. Oxidation kinetics of the alloys by TGA

The oxidation kinetics of the am-Cu_x(Zr_{0.67}Al_{0.33})_{100-x} ($25 \leq x \leq 50$) alloys at 300°C , as determined by TGA, are very similar for all three alloys (see Fig. 2). The initial oxidation regime, as associated with the formation of a dense oxide overlayer, is followed by a second parabolic oxidation stage, according to

$$w(t)^2 = K_p t \quad (1)$$

where K_p is the parabolic oxidation rate constant, w is the mass gain per unit surface area, and t is the oxidation time. Note that the surface area of the Cu-Zr-Al amorphous ribbons was calculated from the geometry of the specimens. All the Cu-Zr-Al ribbons, which were prepared on the same copper wheel by melt-spinning under exactly the same conditions, have a similarly small surface roughness. The K_p values for the oxidation of the am-Cu_x(Zr_{0.67}Al_{0.33})_{100-x} alloys at 300°C , determined by fitting of the experimental growth curves according to Eq. (1) (see Fig. 2), are $3.04 \times 10^{-12} \text{ kg}^2/(\text{m}^4\text{s})$ for am-Cu25, $6.88 \times 10^{-13} \text{ kg}^2/(\text{m}^4\text{s})$ for am-Cu40, and $1.22 \times 10^{-12} \text{ kg}^2/(\text{m}^4\text{s})$ for am-Cu50, respectively. The parabolic growth rate (after initial formation of a dense oxide scale) indicates that the second oxidation stage is diffusion-controlled. It follows that the am-Cu25 alloy with the lowest Cu content has the highest growth rate; the oxidation rate for the am-Cu50 alloy is slightly higher than that of the am-Cu40 alloy.

3.3. Depth-resolved oxide composition by AES depth profiling

The AES-concentration depth profiles of the am-Cu_x(Zr_{0.67}Al_{0.33})_{100-x} alloys oxidized at 250 , 300 and 350°C for 10 h are shown in Fig. 3. A mixed (Zr,Al)-oxide layer with a nominal composition of $(\text{Zr}_{0.67}\text{Al}_{0.33})\text{O}_{1.83}$ (i.e. having the same Al/Zr-ratio of $\frac{1}{2}$ as in the alloy) and an approximate thickness in the range of $5\text{--}55$ nm is formed on the am-Cu25 alloy, independent of the oxidation temperature in the range of $250\text{--}350^{\circ}\text{C}$: see Fig. 3a₁-a₃. A Cu enrichment ('pile-up') in the alloy adjacent to the alloy/oxide interface (due to the synchronous oxidation Zr and Al from the alloy) is only evident for the faster overgrowth of relatively thick oxide layers at the highest oxidation temperature of 350°C . The dissolved oxygen concentration in am-Cu25 alloy at

Table 1

Thermal properties (T_g glass transition temperature, T_x crystallization temperature, and ΔT supercooled liquid regime) of the am-Cu_x(Zr_{0.67}Al_{0.33})_{100-x} ($25 \leq x \leq 50$) alloys as determined by DSC (heating rate $10^{\circ}\text{C}/\text{min}$).

alloy	T_g ($^{\circ}\text{C}$)	T_x ($^{\circ}\text{C}$)	ΔT ($^{\circ}\text{C}$)
am-Cu25	488	509	21
am-Cu40	483	506	23
am-Cu50	487	497	10

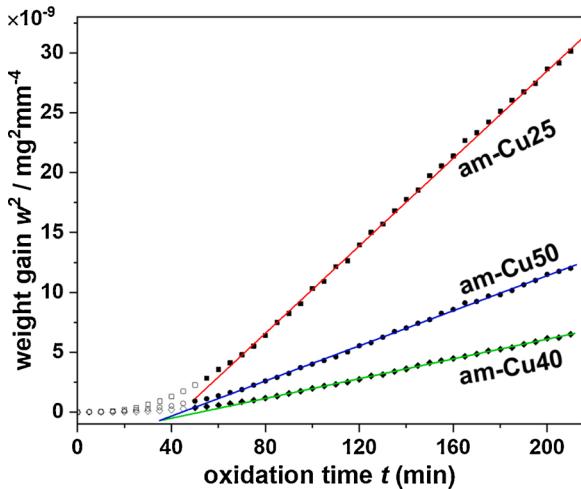


Fig. 2. TGA curves of am-Cu_x(Zr_{0.67}Al_{0.33})_{100-x} alloys (25≤x≤50) during thermal oxidation at 300 °C.

250–350 °C can be neglected.

The depth-resolved compositions of the oxide layers formed on the am-Cu40 and am-Cu50 alloys after the thermal oxidations for 10 h in the range of 250–350 °C are all very similar: compare Fig. 3b₁–b₃ and c₁–c₃. At the lowest oxidation temperature of 250 °C, mixed-(Zr,Al) oxide layers with a nominal composition (Zr_{0.67}Al_{0.33})O_{1.83} and an approximate thickness of ~5 nm are formed on both alloys and only a slight Cu-

enrichment is observed in the alloy underneath: compare Fig. 3b₁ and c₁. Also there are no obvious traces of dissolution and/or inward diffusion of O from the oxide overlayer into the alloy at 250–350 °C. Interestingly, at the higher oxidation temperatures of 300 and 350 °C, a double-layered oxide layer evolves, as composed of a ZrO₂ top layer (thickness: 6–12 nm) and a mixed (Zr,Al)-oxide bottom layer (thickness: 4–24 nm): see Fig. 3b₂–b₃ and c₂–c₃. Notably, the formation of a bilayered oxide overgrowth on the am-Cu40 and am-Cu50 alloys in the range of 300–350 °C is independent of the studied oxidation time (data not shown here). Enrichments of both Cu and Al are observed in the alloy adjacent to the alloy/oxide interface, in particular, for the oxidations of the am-Cu40 and am-Cu50 alloys at 300 °C: see Fig. 3b₂ and c₂. Notably, the Cu enrichment is the most pronounced for the oxidized am-Cu40 at 300–350 °C among the three Cu-Zr-Al amorphous alloys (Fig. 3b₂ vs. a₂ and c₂, Fig. 3b₃ vs. a₃ and c₃).

The approximate thicknesses of the ZrO₂ sublayer (d_{ZrO_2}), the Zr-Al-O sublayer (d_{ZrAlO}), the Cu-enriched layer ($d_{\text{Cu-rich}}$), as well as the respective total oxide layer thicknesses ($d_{\text{ox}} = d_{\text{ZrO}_2} + d_{\text{ZrAlO}}$), as estimated from the AES analyses, are listed in Table 2. The nominal oxide-layer thicknesses formed on the am-Cu_x(Zr_{0.67}Al_{0.33})_{100-x} (25≤x≤50) alloys at the same temperatures decrease in the sequence $r(\text{am-Cu25}) > r(\text{am-Cu50}) > r(\text{am-Cu40})$, in accordance with the TGA analysis (see Sect. 3.2). Continued oxide film growth on the am-Cu40 and am-Cu50 alloys is primarily realized by a thickening of the Zr-Al-O sublayer (i.e. from 2.5 h to 10 h at 350 °C, see Table 2). For identical oxidation conditions, the Cu-enriched zone in the alloy ($d_{\text{Cu-rich}}$) is the thickest for the Cu-rich am-Cu50 alloy, in accordance with its higher oxidation rate (as compared to the am-Cu40 alloy; see Table 2).

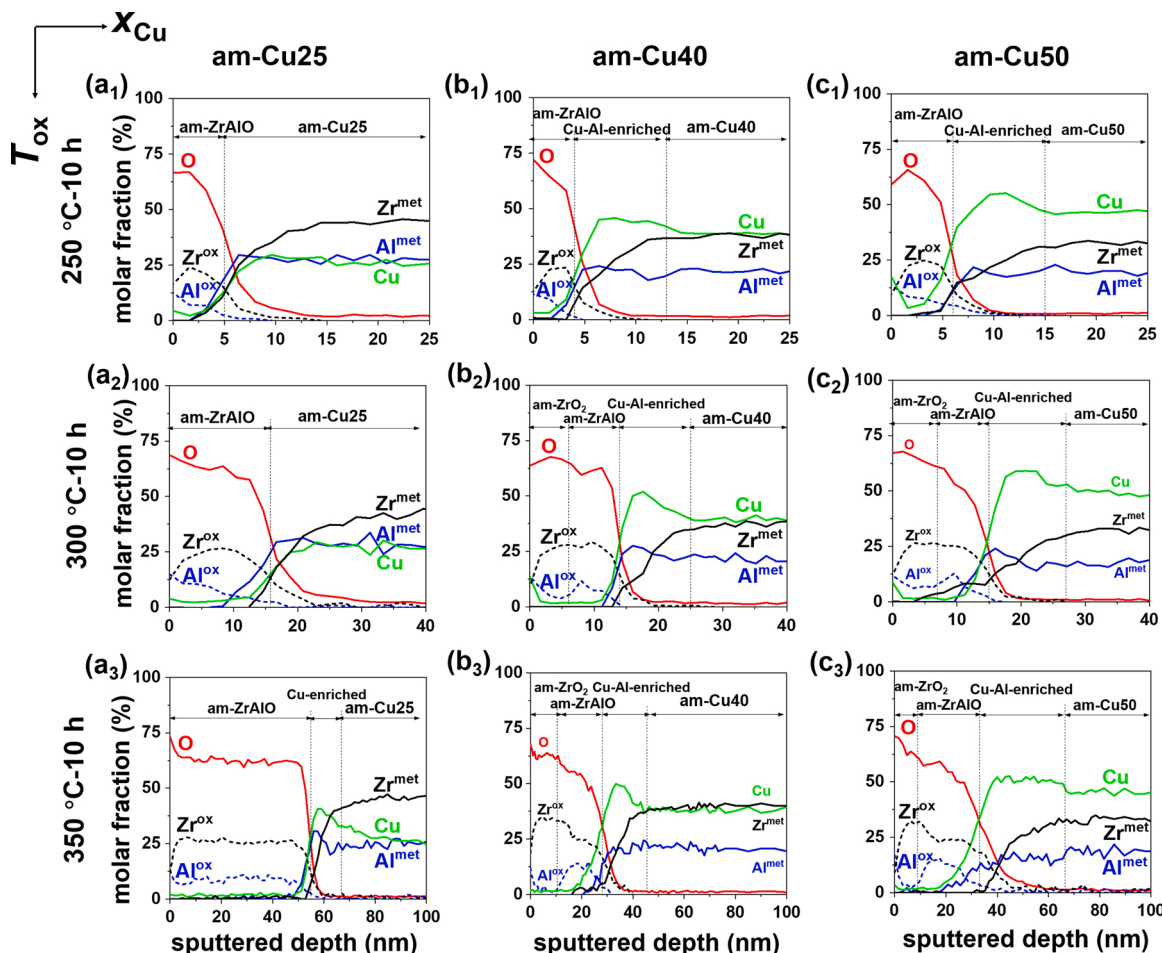


Fig. 3. AES concentration-depth profiles of the am-Cu25 alloy oxidized at (a₁) 250 °C, (a₂) 300 °C, and (a₃) 350 °C for 10 h; the am-Cu40 alloy oxidized at (b₁) 250 °C, (b₂) 300 °C, and (b₃) 350 °C for 10 h; and the am-Cu50 alloy oxidized at (c₁) 250 °C, (c₂) 300 °C, and (c₃) 350 °C for 10 h.

Table 2

Thicknesses of the oxide layers (d_{ox}) [composed of thicknesses of am-ZrO₂ ($d_{Cu-rich}$) and am-ZrAlO (d_{ZrAlO}) sublayers], and Cu-enriched layers ($d_{Cu-rich}$) formed on the am-Cu_x(Zr_{0.67}Al_{0.33})_{100-x} (25 ≤ x ≤ 50) alloys after oxidation at 250 – 350 °C for 10 h.

alloy	d_{ox} (nm)						$d_{Cu-rich}$ (nm)		
	250 °C		300 °C		350 °C		250 °C	300 °C	350 °C
	d_{ox}	d_{ZrO_2}	d_{ZrAlO}	d_{ox}	d_{ZrO_2}	d_{ZrAlO}			
am-Cu25	5	0	16	16	0 (10 h)	55 (10 h)	55 (10 h)	NA	NA
am-Cu40	4	6	8	14	11–13 (2.5 h → 10 h)	11–17 (2.5 h → 10 h)	22–30 (2.5 h → 10 h)	9	11
am-Cu50	6	7	8	15	10–11 (2.5 h → 10 h)	17–23 (2.5 h → 10 h)	27–34 (2.5 h → 10 h)	9	12
									33

Au marker experiments were conducted for the oxidation of am-Cu_x(Zr_{0.67}Al_{0.33})_{100-x} (25 ≤ x ≤ 50) alloys at 350 °C for 2.5 h, followed by AES depth-profiling analyses (see Fig. 4). The pre-deposited ultra-thin (thickness: 2–3 nm) inert Au markers remained on top of the oxide surface, instead of being buried within or below the thickening oxide overlayer. This suggests that oxide-layer growth occurred mainly at the interface between the developing oxide layer and the parent alloy (further designated as the **oxide growth front**) through inward diffusion of oxygen anions (with concurrent outward diffusion of anion vacancies, as generated at the oxide/alloy interface by continuous dissolution of oxygen into the parent alloy), in accordance with the oxidation mechanism for pure Zr metal [54, 55] and Zr-Al alloys [22].

3.4. Microstructure of the oxidized alloys by cross-sectional TEM

The am-Cu_x(Zr_{0.67}Al_{0.33})_{100-x} (25 ≤ x ≤ 50) alloys oxidized at 350 °C for 10 h were also investigated by cross-sectional TEM. The amorphous states of the oxide layer and the parent am-Cu25 alloy are confirmed by the selected area electron diffraction pattern (SAED) (see the inset of Fig. 5a), consistent with the XRD results (see Fig. 1b). As shown in the TEM image of Fig. 5a (with corresponding EDX elemental mapping in Fig. 5b), a uniform and homogenous amorphous oxide layer (thickness: ~54 nm) is formed on the oxidized am-Cu25 alloy. Fig. 5c shows an HRTEM investigation of the interfacial region between the oxide layer and the am-Cu25 substrate, which indicates the existence of nano-sized crystalline domains in the Cu-enriched region of the alloy adjacent to the oxide growth front (see the fast Fourier transform (FFT) in the inset of Fig. 5c).

The cross-sectional TEM analysis of the am-Cu40 alloy oxidized at 350 °C for 10 h is shown in Fig. 6. The SAED of the parent alloy, as shown in the inset of Fig. 6a, confirms the amorphous state of the am-Cu40 alloy, in accordance with XRD analyses (see Fig. 1b). A double-layered oxide composed with individual layer thicknesses of about 13 nm (top) and 15 nm (bottom) are formed on the oxidized am-Cu40 alloy (see Fig. 6a). As revealed from the corresponding EDX elemental mapping (see Fig. 6b), the top oxide sublayer consists of pure ZrO₂, while the bottom oxide sublayer is composed of Zr-Al-O, which is fully consistent with the AES depth profiling results (see Fig. 3b₃). The HRTEM analysis indicates that both the ZrO₂ (top) and Zr-Al-O (bottom) sublayers are TEM amorphous (see Fig. 6c-i). A Cu-Al-enriched region is observable beneath the two amorphous oxide sublayers adjacent to the oxide growth front (see Fig. 6a-b). HRTEM observation indicates that this Cu-Al-enriched layer consists of tiny crystalline Cu₉Al₄ nanograins (see the HRTEM image and FFT in Fig. 6b-ii).

The cross-sectional TEM analysis of the am-Cu50 alloy oxidized at 350 °C for 10 h is shown in the Fig. 7. The amorphous state of the parent am-Cu50 alloy is confirmed by the SAED, as shown in the inset of the Fig. 7a. Similar to the oxidized am-Cu40 alloy, a double-layered oxide, composed of two uniform and homogenous oxide sublayers with thicknesses of 8 nm (top) and 24 nm (bottom), are formed on the oxidized am-Cu50 alloy (see Fig. 7a and the high angle annular dark field (HAADF) image in Fig. 7b). The two oxide sublayers are also amorphous, as evidenced by HRTEM and corresponding FFT analysis (see the inset of Fig. 7c-i). The EDX elemental mapping (see Fig. 7b) and

the AES depth-profiling (see Fig. 3c₃) confirm the homogenous compositions of the two surficial oxide layers as (amorphous) ZrO₂ and (amorphous) (Zr_{0.67}Al_{0.33})O_{1.83}, respectively. A Cu-Al-enriched layer is observed in the alloy adjacent to the oxide growth front, which again contains crystalline Cu₉Al₄ nanograins (see Fig. 7c-ii and FFT of Fig. 7a-iii in the bottom inset Fig. 7c-ii). The Cu-Al-enriched region in the oxidized am-Cu50 alloy is much thicker than that in the oxidized am-Cu40 alloy (Figs. 6a vs. 7 a, and Figs. 6b vs. 7 b), in accordance with the AES results.

4. Discussion

4.1. Microstructure of oxide layers

At the lowest oxidation temperatures of 250 °C, amorphous Zr-Al-O films with a stoichiometric composition of (Zr_{0.67}Al_{0.33})O_{1.83} are formed on top of the am-Cu_x(Zr_{0.67}Al_{0.33})_{100-x} (25 ≤ x ≤ 50) alloys (Fig. 3a₁, b₁ and c₁). This indicates that oxide-layer growth at these relatively low temperatures occurs by synchronous oxidation of Zr and Al from the parent alloy, which complies with the much higher O affinities of Zr and Al as compared to Cu, as well as the deep minimum for the Gibbs energy of formation of the amorphous am-(AlO_{1.5})_y(ZrO₂)_{1-y} phase of fixed composition $y = 0.33$ (corresponding to (Zr_{0.67}Al_{0.33})O_{1.83}), as predicted in the previous study of oxidation of amorphous Zr-Al alloys [25]. As shown in our previous work on the oxidation of crystalline and amorphous binary Zr-Al alloys [22], the formation of an amorphous (Zr,Al)-oxide layer (with the same Al/Zr-ratio as compared to the alloy) results from the continuous dissolution of O into the amorphous alloy matrix at the oxide growth front. Oxide nucleation is triggered if the solubility product zone for the formation of the am-(AlO_{1.5})_y(ZrO₂)_{1-y} phase in the O-dissolution zone is exceeded. The formation of a single-phase crystalline oxide polymorph is bulk-thermodynamically unfavorable, since crystalline ZrO₂ and crystalline Al₂O₃ oxide phases are mutually insoluble within the studied temperature range [25]. The competing formation of phase-segregated single crystalline ZrO₂ and Al₂O₃ oxide phases would require substantial atomic arrangements of Zr and Al in the amorphous alloy, which are kinetically obstructed in the amorphous alloys within the investigated temperature range [25].

At higher oxidation temperatures of 300 and 350 °C, a single-phase am-(Zr_{0.67}Al_{0.33})O_{1.83} oxide overlayer is also found for the oxidized am-Cu25 alloy (Figs. 3a₂-a₃ and 5). However, an am-ZrO₂/am-(Zr_{0.67}Al_{0.33})O_{1.83} bilayered oxide develops on the Cu-rich am-Cu40 and am-Cu50 alloys at 300 °C and 350 °C (Fig. 3c₂-c₃ and b₂-b₃, as well as Figs. 6 and 7). This suggests that, for Cu alloying concentration up to 25 at.%, the presence of Cu in the alloy does not hinder the nucleation and growth of the am-(Zr_{0.67}Al_{0.33})O_{1.83} oxide phase by synchronous oxidation of Zr and Al. However, for higher Cu concentrations, the synchronous oxidation of Zr and Al is hindered, resulting in the formation of a bilayered oxide scale, as explained below.

For the oxidation of amorphous and crystalline Zr-Al alloys [22], the rate-limiting step of the observed parabolic oxidation kinetics could be unambiguously attributed to the diffusional constraints of Zr, Al and dissolved O in the parent crystalline or amorphous alloy directly behind

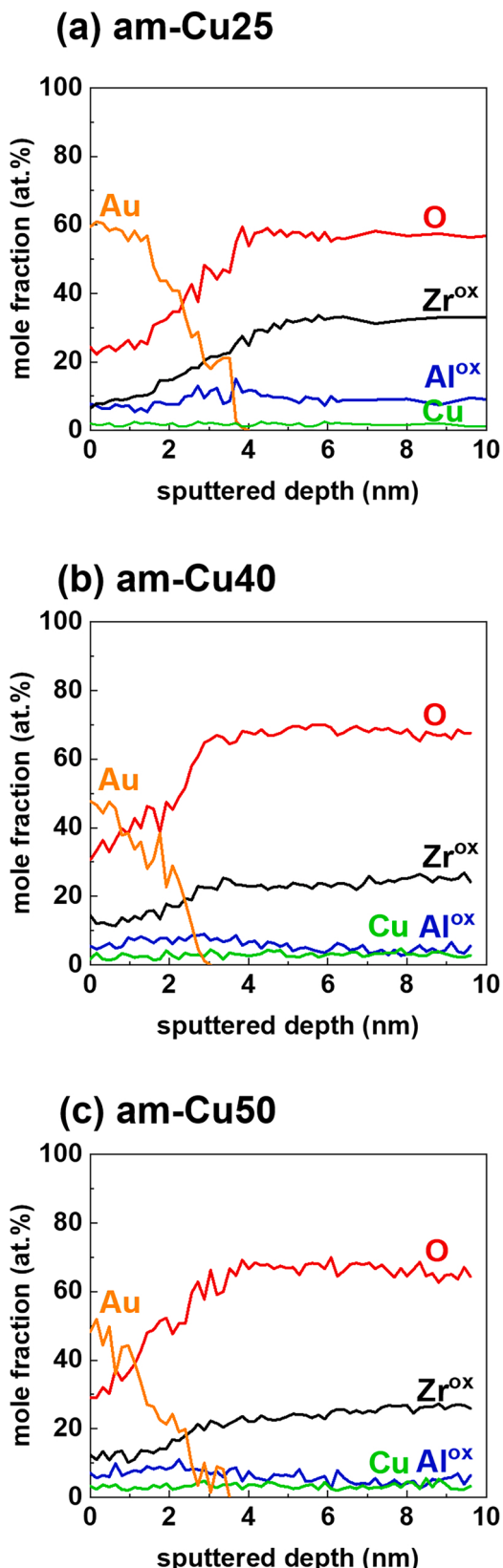


Fig. 4. AES concentration-depth profiles of 2-nm Au-covered (a) am-Cu25, (b) am-Cu40, and (c) am-Cu50 alloys oxidized at 350 °C for 2.5 h.

the oxide growth front. Analogously, for the ternary Cu-Zr-Al alloys under study, the role of Cu on the relative atomic mobilities of Zr, Al and dissolved O in the parent alloy directly behind the oxide growth front should be considered.

The activities of the constituent elements in the amorphous Cu-Zr-Al alloys at 300 °C were calculated via the CALPHAD method using the thermodynamic parameters in Ref. [56], as gathered in Table 3. Since there is no thermodynamic description for the amorphous phase, the activities of the pure elements in the undercooled (configurationally frozen) liquid (below the glass transition temperature T_g) were calculated as an approximation. The chemical activity of Cu strongly increases with the addition of Cu in the amorphous Cu-Zr-Al alloys (Table 3). Note that the chemical activity of Al also increases, though the Al concentration decreases in the amorphous Cu-Zr-Al (Table 3). By comparing the Gibbs energies of formation of possible Cu-Zr [37] and Cu-Al [57] intermetallic phases in the respective compositional range, it follows that Cu has a much higher affinity to Al than to Zr (see Table 4, one order of magnitude difference). This implies that the synchronous oxidation of Zr and Al is strongly disturbed particularly for the oxidations of the Cu-rich am-Cu40 and am-Cu50 ternary alloys. Namely, the relatively strong chemical interaction of Cu with Al will reduce their atomic mobilities (as compared to Zr) in the alloy and can even selectively immobilize Cu and Al atoms by the nucleation of tiny nanocrystalline Cu-Al intermetallic precipitates.

Consequently, only Zr is preferentially oxidized during the initial stages of fast oxidation stage for the Cu-rich am-Cu40 and am-Cu50. The synchronous oxidation of Zr and Al and associated continuous growth of the $(Zr_{0.67}Al_{0.33})O_{1.83}$ bottom layer presumably only dominates after formation of a dense ZrO_2 top layer (during the initial non-parabolic growth stage) with an associated depletion of Zr from the alloy directly behind the oxide growth front (as might be speculated from the AES depth-profiles in Fig. 3). Continuous growth mainly proceeds by a thickening of the $(Zr_{0.67}Al_{0.33})O_{1.83}$ bottom layer during the oxidation stage with a parabolic-type kinetics (Table 2).

Such a transition from synchronous oxidation (of Zr and Al) to preferential oxidation (of Zr) with the addition of Cu can also occur in amorphous Cu-Zr-Al alloys with an Al/Zr ratio other than 0.5. At lower oxidation temperatures, such as room temperature, a synchronous oxidation of Zr and Al tends to occur on the amorphous Cu-Zr-Al alloys irrespective of the Cu content, forming a very thin (<5 nm) amorphous Zr-Al-O oxide.

4.2. Microstructure of Cu-enriched regions

Formation of an (Zr,Al)-oxide phase at the inwardly migrating oxide growth front by synchronous oxidation of Zr and Al requires continuous diffusion of Cu into the interior of the alloy. If the diffusion of expelled Cu from the alloy at the oxide growth is much slower than the rate of the inwardly moving growth front, Cu will be piled up directly behind the oxide growth front (analogous to the pile-up of Cr for the high-temperature oxidation of NiAlCr alloys [19]). Indeed, the AES depth-profiling and TEM analyses (Figs. 3, 5–7) evidence such pile-up of Cu directly behind the oxide growth front for the oxidation of the am-Cu_x(Zr_{0.67}Al_{0.33})_{100-x} (25 ≤ x ≤ 50) alloys towards higher temperatures. A higher oxidation temperature results in a higher oxidation rate and thus a faster inward migration of the growth front. It thus results in a distinct Cu enrichment in the alloy directly behind the oxide growth front towards higher oxidation temperatures, which is most pronounced for the oxidation of the am-Cu40 alloy.

The GFA of the amorphous Cu-Zr-Al alloy system, as reflected by the temperature of supercooled liquid region ($\Delta T = T_x - T_g$), from previous studies [13, 49, 51, 53, 58–61] and the present work (see Table 1, c.f. Fig. 1c) are shown in Fig. 8. It follows that the Cu enrichment in the alloy adjacent to the oxide growth front leads to a reduced GFA. The ΔT of the Cu-enriched region of am-Cu25 alloy is relatively large, whereas ΔT of Cu-enriched regions of am-Cu40 and am-Cu50 alloys becomes negligible

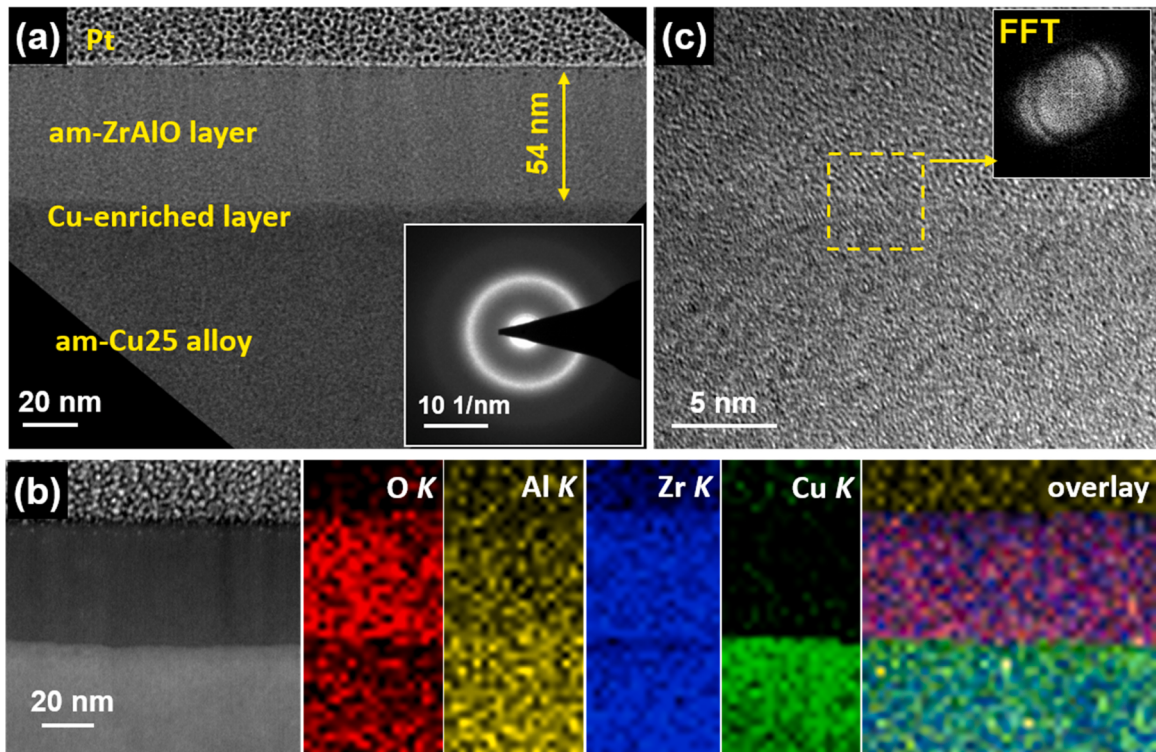


Fig. 5. TEM investigations of the am-Cu25 alloy oxidized at 350 °C for 10 h: (a) cross-sectional TEM image and the corresponding SAED shown in the inset, (b) HAADF image and EDX elemental mapping of the oxide layer region, and (c) HRTEM of the interfacial region between the oxide layer and the parent am-Cu25 alloy, and the corresponding FFT shown in the inset.

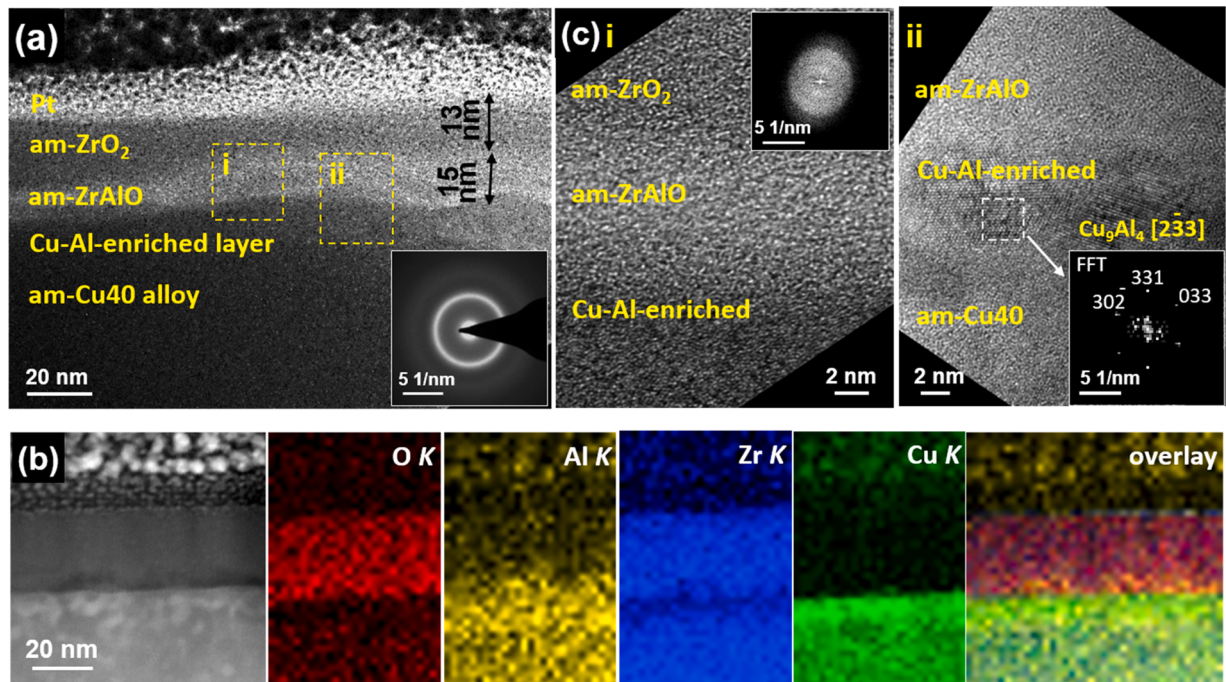


Fig. 6. TEM investigations of the am-Cu40 alloy oxidized at 350 °C for 10 h: (a) cross-sectional TEM image and the corresponding SAED shown in the inset, (b) HAADF image and EDX elemental mapping of the oxide layer, and (c) HRTEM images of the marked regions i and ii in (a) and the corresponding FFTs shown in the inset.

small. As a result, the less distinct Cu-enriched layer in the am-Cu25 alloy oxidized at 350 °C for 10 h preserves its initial amorphous state (Fig. 5b); the more pronounced Cu-enriched layers in the am-Cu40 and am-Cu50 alloys oxidized at 350 °C for 10 h have partially transformed

into a crystalline state by the precipitation of intermetallic nanocrystallites (Figs. 6b and 7b). Only a limited number of stable ternary Cu-Zr-Al intermetallic phases, e.g. τ_3 ($\text{Cu}_{28}\text{Zr}_{51}\text{Al}_{21}$), τ_4 (Cu_2ZrAl) and τ_5 ($\text{Cu}_{36}\text{Zr}_{38}\text{Al}_{26}$) can form, all of which are far away from the nominal

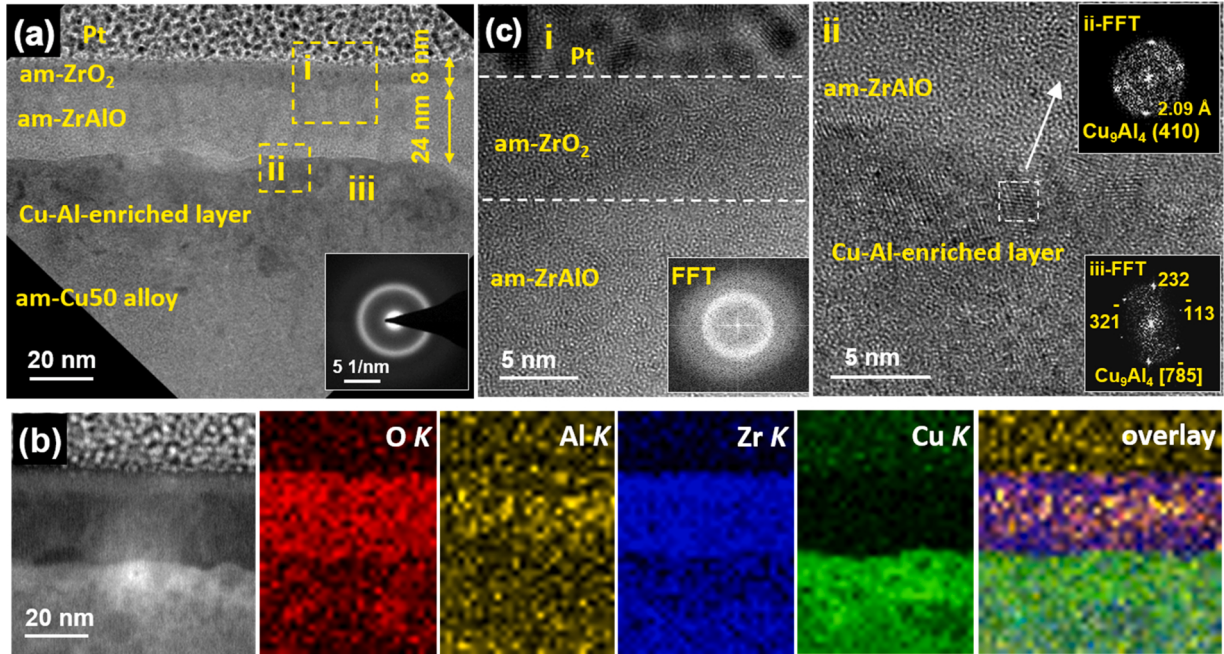


Fig. 7. TEM investigations of the am-Cu50 alloy oxidized at 350 °C for 10 h: (a) cross-sectional TEM image and the corresponding SAED shown in the inset, (b) HAADF image and EDX elemental mapping of the oxide layer, and (c) HRTEM images of the marked regions i and ii in (a) and the corresponding FFTs shown in the inset.

Table 3

Thermodynamic activities a of various elements in the am-Cu_x(Zr_{0.67}Al_{0.33})_{100-x} alloys ($25 \leq x \leq 50$) at 300 °C.

alloy	a_{Cu}	a_{Zr}	a_{Al}
am-Cu25	5.18×10^{-3}	2.58×10^{-2}	6.33×10^{-10}
am-Cu40	4.12×10^{-2}	5.22×10^{-3}	8.03×10^{-10}
am-Cu50	1.14×10^{-1}	1.17×10^{-3}	1.30×10^{-9}

Table 4

Gibbs energies of formation $\Delta G_f^0(T)$ of possible Cu-Zr and Cu-Al intermetallic compounds in the composition range of the Cu-Al-enriched region in the oxidized am-Cu40 and am-Cu50 alloys.

intermetallic phase	Cu (at. %)	$\Delta G_f^0(T)$ (J/mol)	$\Delta G_f^0(300^\circ\text{C})$ [kJ/mol Zr(Al)]
Cu-Zr	CuZr	50.0	-12442-2.703T
	Cu ₁₀ Zr ₇	58.8	-16133-1.905T
	Cu ₂₄ Zr ₁₃	64.9	-17216+1.121T
Cu-Al	Cu ₂ Zr	66.7	-17659+1.535T
	Cu ₃ Al ₂	60.0	-106700+3T
	Cu ₂ Al	66.7	-280501+379.6T-52TlnT
	Cu ₉ Al ₄	69.2	-200460-58.5T

compositions in the Cu-enriched zones of the oxidized am-Cu40 and am-Cu50 alloys (Fig. 8) [12, 51]. Possible binary Cu-Zr and Cu-Al intermetallic phases in the corresponding compositional range, as well as their Gibbs energies of formation (ΔG_f) [37, 57], are collected in Table 4 (as derived from thermodynamic assessments of Cu-Zr [62] and Cu-Al binary alloys [63]). The Cu₉Al₄ phase is thermodynamically preferred (having the lowest ΔG_f of -760.5 kJ/mol Al at 300 °C; see Table 4). Indeed, the TEM analysis (Figs. 6 and 7) indicates the formation of crystalline Cu₉Al₄ nanograins in the Cu-enriched zone for the oxidized am-Cu40 and am-Cu50 alloys. The Cu-Al-enriched layer of am-Cu50 is thicker than that of the am-Cu40 alloy (Table 2, Figs. 6 and 7), as attributed to the higher activities of both Cu and Al in the initial am-Cu50 alloy (Table 3).

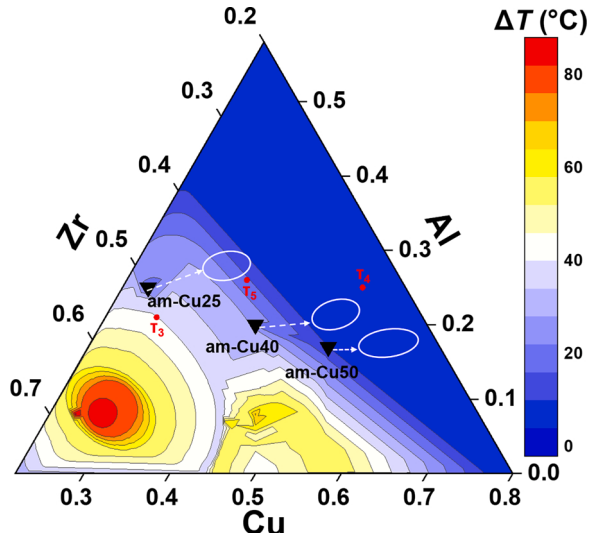


Fig. 8. The supercooled liquid temperature region (ΔT) of the am-CuZrAl alloys [13, 49, 51, 53, 58–61]. Red points represent the ternary Cu-Zr-Al intermetallic phases in the composition range of this GFA diagram: τ_3 (Cu₂₈Zr₅₁Al₂₁), τ_4 (Cu₂ZrAl) and τ_5 (Cu₃₆Zr₃₈Al₂₆). The areas corresponding to the Cu-enriched regions in the oxidized am-CuZrAl alloys are shown in the white circles. (For interpretation of the references to colour in this figure legend, the reader is referred to the web version of this article).

4.3. Oxidation kinetics

After initial formation of a dense oxide scale, the oxidation kinetics of three amorphous Cu-Zr-Al alloys in the second oxidation stage follow a diffusion-controlled parabolic growth law. Au marker experiments indicate that oxide layer growth during the parabolic growth stage occurs by the formation of new oxide phase at the interface between the developing oxide layer and the parent alloy, independent of the alloy composition. The am-Cu25 alloy with the lowest Cu content has the

highest growth rate; the oxidation rate for the am-Cu50 alloy is slightly higher than that of the am-Cu40 alloy.

As discussed in Sect. 4.1, the relatively strong chemical interaction of Cu with Al reduces their atomic mobilities as compared to Zr and may even immobilize Cu and Al by the nucleation of tiny intermetallic precipitates in the Cu-enriched zone directly behind the oxide growth front. Namely, both the required inward diffusion of Cu and the synchronous oxidation of Zr and Al are suppressed in the Cu-enriched zone directly behind the oxide growth front. This rationalizes the slower parabolic growth rates of the Cu-rich am-Cu40 and am-Cu50 alloys, as compared to the am-Cu25 alloy. It even explains why the parabolic oxidation rate of the am-Cu40 alloy is slightly lower than that of the am-Cu50 alloy, since the Cu-enrichment (pile-up) directly behind the oxide growth front is more pronounced for the oxidation of the am-Cu40 alloy at 300 °C and 350 °C.

5. Conclusions

The competition between synchronous oxidation and preferential oxidation of Zr and/or Al in amorphous alloys of $\text{Cu}_x(\text{Zr}_{0.67}\text{Al}_{0.33})_{100-x}$ ($25 \leq x \leq 50$) has been investigated systematically to reveal the role of the addition of a noble alloy constituent (*here*: Cu) on the oxidation mechanism of amorphous ternary alloys.

At the lowest oxidation temperature of 250 °C, single-phase amorphous Zr-Al-O films with a fixed stoichiometric composition of $(\text{Zr}_{0.67}\text{Al}_{0.33})\text{O}_{1.83}$ are formed on top of the am-Cu $_x$ (Zr $_{0.67}$ Al $_{0.33}$) $_{100-x}$ alloys, independent of the Cu alloying content in the range of 25–50 at. %. Hence, oxide-layer growth at relatively low temperatures occurs by synchronous oxidation of Zr and Al from the parent alloy, which is thermodynamically preferred due to the favorable nucleation of the am-(Zr $_{0.67}$ Al $_{0.33}$)O $_{1.83}$ oxide phase.

The effect of Cu addition on the oxidation behavior becomes evident for the oxidations of the Cu-rich alloys towards higher oxidation temperatures of 300 °C and 350 °C. For these elevated temperatures, synchronous oxidation of Zr and Al with concurrent formation of a single-phase am-(Zr $_{0.67}$ Al $_{0.33}$)O $_{1.83}$ overlayer only occurs for Cu alloying contents up to 25 at. %. An am-ZrO $_2$ /am-(Zr $_{0.67}$ Al $_{0.33}$)O $_{1.83}$ bilayered oxide develops on the Cu-Zr-Al amorphous alloys with higher Cu alloying contents of 40 at. % and 50 at. %. For such relatively high Cu alloying contents, the relatively strong chemical interaction of Cu with Al will reduce their atomic mobilities (as compared to Zr) in the alloy and selectively immobilizes Cu and Al atoms from oxidation by the nucleation of tiny nanocrystalline Cu-Al intermetallic precipitates at the oxide growth front. Consequently, the synchronous oxidation of Zr and Al becomes strongly disturbed, and only Zr is preferentially oxidized during the initial stages of fast non-parabolic oxidation for the Cu-rich am-Cu40 and am-Cu50. During the subsequent oxidation stage with a parabolic-type kinetics (after formation of a dense ZrO $_2$ top layer), continuous oxide growth mainly proceeds by a thickening of the (Zr $_{0.67}$ Al $_{0.33}$)O $_{1.83}$ bottom layer.

Both the required inward diffusion of Cu and the synchronous oxidation of Zr and Al are suppressed in the Cu-enriched zone directly behind the oxide growth front. Therefore, the preferential oxidation of Zr in am-Cu40 and am-Cu50 show much slower oxidation rates as compared to the am-Cu25 alloy. The parabolic oxidation rate of the am-Cu40 alloy is slightly lower than that of the am-Cu50 alloy, since the Cu-enrichment (pile-up) at the oxide growth front is more pronounced for the oxidation of the am-Cu40 alloy.

Strong Cu enrichment in the alloy adjacent to the oxide growth front leads to a reduced glass forming ability. The less distinct Cu-enriched layer in the oxidized am-Cu25 alloy preserves its initial amorphous state, whereas the more pronounced Cu-enriched layers in the oxidized am-Cu40 and am-Cu50 alloys have partially transformed into a crystalline state by the precipitation of intermetallic nanocrystallites.

These findings reveal a change in oxidation mode of amorphous ternary Cu $_x$ (Zr $_{0.67}$ Al $_{0.33}$) $_{100-x}$ ($25 \leq x \leq 50$) alloys from synchronous to

preferential oxidation for Cu concentrations >25 at. %. The crucial role of noble alloy constituents (*here*: Cu) on the oxidation behavior of ternary alloys is thus disclosed and may provide new perspectives for surface engineering of ternary alloys by defined pre-oxidation treatments.

Data availability statement

All data included in this study are available upon request by contact with the corresponding author.

CRediT authorship contribution statement

Yifei Xu: Investigation, Formal analysis, Visualization, Writing - original draft. **Lars P.H. Jeurgens:** Conceptualization, Writing - review & editing. **Hong Bo:** Methodology, Software. **Luchan Lin:** Investigation. **Shengli Zhu:** Resources. **Yuan Huang:** Software. **Yongchang Liu:** Project administration. **Junwei Qiao:** Resources. **Zumin Wang:** Conceptualization, Writing - review & editing, Funding acquisition, Project administration.

Declaration of competing interest

The authors report no declarations of interest.

Acknowledgements

This work was supported by the National Natural Science Foundation of China (No. 51571148 and 51971153), and the National Key Research and Development Program of China (No. 2017YFE0302600 and No. 2017YFB0701801). Dr. Luchan Lin acknowledges funding from the European Union's Horizon 2020 research and innovation program under the Marie Skłodowska-Curie grant agreement number 754364. The Empa electron microscopy center, as well as Empa laboratory for transport at nanoscale interfaces, are acknowledged for providing access to the FIB and TEM.

References

- [1] W. Yao, Q.P. Cao, S.Y. Liu, X.D. Wang, H.J. Fecht, A. Caron, D.X. Zhang, J.Z. Jiang, Tailoring nanostructured Ni-Nb metallic glassy thin films by substrate temperature, *Acta Mater.* 194 (2020) 13–26.
- [2] D. Sorensen, E. Hintsala, J. Stevick, J. Pischar, B. Li, D. Kiener, J.C. Myers, H. Jin, J. Liu, D. Stauffer, A.J. Ramirez, R.O. Ritchie, Intrinsic toughness of the bulk-metallic glass Vitreloy 105 measured using micro-cantilever beams, *Acta Mater.* 183 (2020) 242–248.
- [3] N.T. Panagiotopoulos, K. Georgarakis, A.M. Jorge Jr, M. Aljerf, W.J. Botta, A.L. Greer, A.R. Yavari, Advanced ultra-light multifunctional metallic-glass wave springs, *Mater. Des.* 192 (2020), 108770.
- [4] L. Zhao, K.C. Chan, S.H. Chen, S.D. Feng, D.X. Han, G. Wang, Tunable tensile ductility of metallic glasses with partially rejuvenated amorphous structures, *Acta Mater.* 169 (2019) 122–134.
- [5] K.J. Laws, D. Granata, J.F. Löfller, Alloy design strategies for sustained ductility in Mg-based amorphous alloys – tackling structural relaxation, *Acta Mater.* 103 (2016) 735–745.
- [6] J.W. Qiao, H.L. Jia, P.K. Liaw, Metallic glass matrix composites, *Mater. Sci. Eng., R* 100 (2016) 1–69.
- [7] P. Thurnheer, F. Haag, J.F. Löfller, Time-resolved measurement of shear-band temperature during serrated flow in a Zr-based metallic glass, *Acta Mater.* 115 (2016) 468–474.
- [8] H.-R. Jiang, B. Bochtlar, M. Frey, Q. Liu, X.-S. Wei, Y. Min, S.S. Riegler, D.-D. Liang, R. Busch, J. Shen, Equilibrium viscosity and structural change in the Cu $_{47.5}$ Zr $_{45.1}$ Al $_{7.4}$ bulk glass-forming liquid, *Acta Mater.* 184 (2020) 69–78.
- [9] Z. Huang, Z. Wu, X. Cheng, Z. Zhang, G. Xie, Bulk metallic glass composites with high strength and electrical conductivity by sintering Cu-coated CuZrAl glassy powder, *J. Alloys. Compd.* 841 (2020), 155723.
- [10] R. Rashidi, M. Malekan, R. Gholamipour, Crystallization kinetics of Cu $_{47}$ Zr $_{47}$ Al $_6$ and (Cu $_{47}$ Zr $_{47}$ Al $_6$) $_{99}$ Sn $_1$ bulk metallic glasses, *J. Non-Cryst. Solids* 498 (2018) 272–280.
- [11] K. Pajor, T. Koziel, G. Cios, P. Błyskun, P. Bała, A. Zielińska-Lipięc, Glass forming ability of the Zr $_{50}$ Cu $_{40}$ Al $_1$ alloy with two oxygen levels, *J. Non-Cryst. Solids* 496 (2018) 42–47.

- [12] F.G. Courry, W.J. Botta, C. Bolfarini, C.S. Kominami, M.J. Kaufman, The effect of oxygen on the microstructural evolution in crystallized Cu–Zr–Al metallic glasses, *Intermetallics* 65 (2015) 51–55.
- [13] K.R. Lim, M.P. Jin, S.J. Sang, S.Y. Kim, S.J. Kim, E.S. Lee, W.T. Kim, A. Gebert, J. Eckert, D.H. Kim, Effect of thermal stability of the amorphous substrate on the amorphous oxide growth on Zr–Al–(Cu,Ni) metallic glass surfaces, *Corros. Sci.* 73 (13) (2013) 1–6.
- [14] M. Zhang, L. Deng, D. Yao, J.S. Jin, X.Y. Wang, Multilayered scale formation during Zr-based metallic glass oxidation in the supercooled liquid region, *Corros. Sci.* 111 (2016) 556–567.
- [15] K.N. Sasidhar, S.R. Meka, Room temperature oxide-film formation by oxygen dissolution induced surface directed spinodal decomposition in stainless steel, *Corros. Sci.* 166 (2020), 108433.
- [16] Z.Q. Xu, Y.F. Xu, A. Zhang, J.Y. Wang, Z.M. Wang, Oxidation of amorphous alloys, *J. Mater. Sci. Technol.* 34 (11) (2018) 1977–2005.
- [17] Z. Lei, X. Liu, Y. Wu, H. Wang, S. Jiang, S. Wang, X. Hui, Y. Wu, B. Gault, P. Kontis, D. Raabe, L. Gu, Q. Zhang, H. Chen, H. Wang, J. Liu, K. An, Q. Zeng, T.-G. Nieh, Z. Lu, Enhanced strength and ductility in a high-entropy alloy via ordered oxygen complexes, *Nature* 563 (7732) (2018) 546–550.
- [18] K.N. Sasidhar, S.R. Meka, Spinodal decomposition during isothermal gas-solid equilibration – its effects and implications, *Acta Mater.* 161 (2018) 266–272.
- [19] T.J. Nijdam, L.P.H. Jeurgens, W.G. Sloof, Modelling the thermal oxidation of ternary alloys – compositional changes in the alloy and the development of oxide phases, *Acta Mater.* 51 (18) (2003) 5295–5307.
- [20] S. Siol, C. Beall, N. Ott, M. Döbeli, M. González-Castaño, R. Wick-Joliat, S.D. Tilley, L.P.H. Jeurgens, P. Schmutz, C. Cancellieri, Anodizing of self-passivating W_xTi_{1-x} precursors for $W_xTi_{1-x}O_n$ oxide alloys with tailored stability, *ACS Appl. Mater. Interfaces* 11 (9) (2019) 9510–9518.
- [21] W. Mao, R.W.A. Hendrikx, W.G. Sloof, Prediction of oxide phases formed upon internal oxidation of advanced high-strength steels, *Oxid. Met.* 89 (5) (2018) 531–549.
- [22] Y.F. Xu, L.P.H. Jeurgens, Y. Huang, C. Li, Y.C. Liu, Z.M. Wang, Effect of structural order on oxidation kinetics and oxide phase evolution of Al–Zr alloys, *Corros. Sci.* 165 (2020), 108407.
- [23] K. Weller, Z.M. Wang, L.P.H. Jeurgens, E.J. Mittemeijer, Oxidation kinetics of amorphous Al_xZr_{1-x} alloys, *Acta Mater.* 103 (2016) 311–321.
- [24] K. Weller, T. Suter, Z.M. Wang, L.P.H. Jeurgens, E.J. Mittemeijer, The effect of pre-oxidation treatment on the corrosion behavior of amorphous $Al_{1-x}Zr_x$ solid-solution alloys, *Electrochim. Acta* 188 (2016) 31–39.
- [25] K. Weller, Z.M. Wang, L.P.H. Jeurgens, E.J. Mittemeijer, Thermodynamics controls amorphous oxide formation: exclusive formation of a stoichiometric amorphous $(Al_{0.33}Zr_{0.67})O_{1.83}$ phase upon thermal oxidation of Al–Zr, *Acta Mater.* 94 (2015) 134–142.
- [26] K. Weller, L.P.H. Jeurgens, Z.M. Wang, E.J. Mittemeijer, Thermal oxidation of amorphous $Al_{0.44}Zr_{0.56}$ alloys, *Acta Mater.* 87 (2015) 187–200.
- [27] I.L. Soroka, J. Vegelius, P.T. Korelis, A. Fallberg, S.M. Butorin, B. Hjörvarsson, Structural stability and oxidation resistance of amorphous Zr–Al alloys, *J. Nucl. Mater.* 401 (1–3) (2010) 38–45.
- [28] Y.F. Xu, L.P.H. Jeurgens, P. Schützendübe, S.L. Zhu, Y. Huang, Y.C. Liu, Z.M. Wang, Effect of atomic structure on preferential oxidation of alloys: amorphous versus crystalline Cu–Zr, *J. Mater. Sci. Technol.* 40 (2020) 128–134.
- [29] Y.F. Xu, Y.Y. Chen, P. Schützendübe, S.L. Zhu, Y. Huang, Z.Q. Ma, Y.C. Liu, Z.M. Wang, Thermal oxidation of amorphous Cu_xZr_{1-x} alloys: role of composition-dependent thermodynamic stability, *Appl. Surf. Sci.* 503 (2020), 144376.
- [30] Y.F. Xu, X.Y. Liu, L. Gu, J.Y. Wang, P. Schützendübe, Y. Huang, Y.C. Liu, Z.M. Wang, Natural oxidation of amorphous Cu_xZr_{1-x} alloys, *Appl. Surf. Sci.* 457 (2018) 396–402.
- [31] M. Kotrlavá, P. Zeman, Š. Zuzjaková, M. Zítek, On crystallization and oxidation behavior of $Zr_{54}Cu_{46}$ and $Zr_{27}Hf_{27}Cu_{46}$ thin-film metallic glasses compared to a crystalline $Zr_{54}Cu_{46}$ thin-film alloy, *J. Non-Cryst. Solids* 500 (2018) 475–481.
- [32] B.B. Liu, C.Y. Han, F. Ye, Adjustment of temperature coefficient of electrical resistivity in $Cu_{66}Zr_{34}$ metallic glass through surface oxidation induced phase decomposition, *Corros. Sci.* 125 (2017) 166–174.
- [33] K.R. Lim, J.M. Park, S.H. Park, M.Y. Na, K.C. Kim, W.T. Kim, D.H. Kim, Oxidation induced amorphous stabilization of the subsurface region in Zr–Cu metallic glass, *Appl. Phys. Lett.* 104 (3) (2014).
- [34] G. Wu, K. Dash, M.L. Galano, K.A.Q. O'Reilly, Oxidation studies of Al alloys: part I Al–Cu (liquid phase) alloy, *Corros. Sci.* 157 (2019) 41–50.
- [35] J. Tao, Surface Composition and Corrosion Behavior of an Al–Cu Alloy, Université Pierre et Marie Curie, Paris, 2016.
- [36] E. Hinton, W. Griffiths, N. Green, Comparison of oxide thickness of aluminium and the effects of selected alloying additions, *Mater. Sci. Forum* 765 (2013) 180–184.
- [37] S.H. Zhou, R.E. Napolitano, Phase stability for the Cu–Zr system: first-principles, experiments and solution-based modeling, *Acta Mater.* 58 (6) (2010) 2186–2196.
- [38] S.Y. Luo, J.H. Li, Y.Y. Cui, Y. Dai, B.X. Liu, Monte Carlo simulations to study the forming ability and atomic configuration of the Cu–Al amorphous alloys, *Intermetallics* 25 (2012) 109–114.
- [39] H.B. Yan, F.X. Gan, D.Q. Huang, Evaporated Cu–Al amorphous alloys and their phase transition, *J. Non-Cryst. Solids* 112 (1) (1989) 221–227.
- [40] N.M. Mayer, H. Hoffmann, A. Schäfer, Crystallization of amorphous Al–Cu films, *Thin Solid Films* 88 (3) (1982) 225–238.
- [41] A. Lambrecht, H. Leitz, J. Hasse, Superconducting amorphous Al–Cu films of high stability, *Z. Phys. B: Condens. Matter* 38 (1) (1980) 35–41.
- [42] H. Leitz, H.J. Nowak, M.S. El-Dessouki, V.K. Srivastava, W. Buckel, Superconductivity and structure of quench condensed Al–Cu-films, *Z. Phys. B: Condens. Matter* 29 (3) (1978) 199–202.
- [43] K.R. Lim, J.M. Park, S.J. Kim, E.S. Lee, W.T. Kim, A. Gebert, J. Eckert, D.H. Kim, Enhancement of oxidation resistance of the supercooled liquid in Cu–Zr-based metallic glass by forming an amorphous oxide layer with high thermal stability, *Corros. Sci.* 66 (2013) 1–4.
- [44] W.H. Cao, J.L. Zhang, C.H. Shek, The oxidation behavior of $Cu_{42}Zr_{42}Al_8Ag_8$ bulk metallic glasses, *J. Mater. Sci.* 48 (3) (2013) 1141–1146.
- [45] K.R. Lim, W.T. Kim, E.S. Lee, S.S. Jee, S.Y. Kim, D.H. Kim, A. Gebert, J. Eckert, Oxidation resistance of the supercooled liquid in $Cu_{50}Zr_{50}$ and $Cu_{46}Zr_{46}Al_8$ metallic glasses, *J. Mater. Res.* 27 (8) (2012) 1178–1186.
- [46] J.L. Zhang, W.H. Cao, C.H. Shek, Silver mushroom induced by oxidation in $Cu_{42}Zr_{42}Al_8Ag_8$ metallic glasses, *J. Alloys Compd.* 509 (Suppl. 1) (2011) S219–S222.
- [47] W. Kai, P.C. Kao, P.C. Lin, I.F. Ren, J.S.C. Jang, Effects of Si addition on the oxidation behavior of a Cu–Zr-based bulk metallic alloy, *Intermetallics* 18 (10) (2010) 1994–1999.
- [48] W. Kai, I.F. Ren, P.C. Kao, R.F. Wang, C.P. Chuang, M.W. Freels, P.K. Liaw, Air-oxidation of a $Cu_{45}Zr_{45}Al_5Ag_5$ bulk metallic glass, *Adv. Eng. Mater.* 11 (5) (2009) 380–386.
- [49] W. Kai, T.H. Ho, H.H. Hsieh, Y.R. Chen, D.C. Qiao, F. Jiang, G. Fan, P.K. Liaw, Oxidation behavior of CuZr-based glassy alloys at 400 °C to 500 °C in dry air, *Metall. Mater. Trans. A* 39 (8) (2008) 1838–1846.
- [50] Z.P. Hu, Y.F. Xu, Y.Y. Chen, P. Schützendübe, J.Y. Wang, Y. Huang, Y.C. Liu, Z.M. Wang, Anomalous formation of micrometer-thick amorphous oxide surficial layers during high-temperature oxidation of $ZrAl_2$, *J. Mater. Sci. Technol.* 35 (7) (2019) 1479–1484.
- [51] D. Wang, H. Tan, Y. Li, Multiple maxima of GFA in three adjacent eutectics in Zr–Cu–Al alloy system – a metallographic way to pinpoint the best glass forming alloys, *Acta Mater.* 53 (10) (2005) 2969–2979.
- [52] Q.S. Zhang, W. Zhang, G.Q. Xie, A. Inoue, Glass-forming ability and mechanical properties of the ternary Cu–Zr–Al and quaternary Cu–Zr–Al–Ag bulk metallic glasses, *Mater. Trans.* 48 (7) (2007) 1626–1630.
- [53] T.L. Cheung, C.H. Shek, Thermal and mechanical properties of Cu–Zr–Al bulk metallic glasses, *J. Alloys. Compd.* 434–435 (2007) 71–74.
- [54] G. Bakradze, L.P.H. Jeurgens, T. Acarturk, U. Starke, E.J. Mittemeijer, Atomic transport mechanisms in thin oxide films grown on zirconium by thermal oxidation, as-derived from O^{18} -tracer experiments, *Acta Mater.* 59 (20) (2011) 7498–7507.
- [55] R. Prescott, M.J. Graham, The formation of aluminum oxide scales on high-temperature alloys, *Oxid. Met.* 38 (3) (1992) 233–254.
- [56] H. Bo, J. Wang, S. Jin, H.Y. Qi, X.L. Yuan, L.B. Liu, Z.P. Jin, Thermodynamic analysis of the Al–Cu–Zr bulk metallic glass system, *Intermetallics* 18 (12) (2010) 2322–2327.
- [57] I. Ansara, A.T. Dinsdale, M.H. Rand, Definition of thermodynamical and thermophysical properties to provide a database for the development of new light alloys, COST 507-Final Report: Thermochemical Database for Light Metal Alloys, Brussels, 1998.
- [58] J. Dąbrowska, L. Perriere, M. Stygar, W. Kucza, Ł. Klita, M. Danielewski, Oxidation behavior of $Zr_{43}Cu_{45}Al_{12}$ bulk metallic glass at 400–525 °C in air atmosphere, *J. Mater. Eng. Perform.* 24 (12) (2015) 4863–4869.
- [59] W. Kai, P.C. Lin, W.S. Chen, C.P. Chuang, P.K. Liaw, H.H. Huang, H.H. Hsieh, Air-oxidation of a $Zr_{50}Cu_{43}Al_7$ bulk metallic glass at 400–500 °C, *Corros. Sci.* 64 (2012) 98–104.
- [60] E.S. Park, D.H. Kim, Phase separation and enhancement of plasticity in Cu–Zr–Al–Y bulk metallic glasses, *Acta Mater.* 54 (10) (2006) 2597–2604.
- [61] Y. Wu, T. Nagase, Y. Umakoshi, Effect of crystallization behavior on the oxidation resistance of a Zr–Al–Cu metallic glass below the crystallization temperature, *J. Non-Cryst. Solids* 352 (28–29) (2006) 3015–3026.
- [62] D. Arias, J.P. Abriata, Cu–Zr (Copper-Zirconium), *J. Phase Equilibria Diffus.* 11 (5) (1990) 452–459.
- [63] M. Mishler, V. Ouvarov-Bancalero, S.H. Chae, L. Nguyen, C.-U. Kim, Intermetallic compound growth and stress development in Al–Cu diffusion couple, *J. Electron. Mater.* 47 (1) (2018) 855–865.